Energy Harvesting From CO2 Emissions: The Role of Gas Concentration, Flow, and Supporting Electrolyte

Advanced Sustainable Systems

ADVANCED SUSTAINABLE SYSTEMS
www.advsustainsys.com

RESEARCH ARTICLE OPEN ACCESS

Energy Harvesting From CO_2 Emissions: The Role of Gas Concentration, Flow, and Supporting Electrolyte

Simone Martellone[1,2] | Davide Molino[1,2] | Pietro Zaccagnini[1,2] | Giuseppe Ferraro[1,2] | Silvia Di Martino[2] | Sergio Bocchini[1,2] | Andrea Lamberti[1,2]

[1]Dipartimento di Scienze Applicate e Tecnologia, Politecnico di Torino, Torino, Italy | [2]Centre for Sustainable and Future Technologies, Istituto Italiano di Tecnologia, Torino, Italy

Correspondence: Davide Molino (davide.molino@iit.it) | Andrea Lamberti (andrea.lamberti@polito.it)

Received: 24 April 2026 | **Revised:** 6 July 2026 | **Accepted:** 9 July 2026

Keywords: carbon dioxide | energy harvesting | ionic liquids

ABSTRACT

This work explores an innovative approach to convert CO_2 into a valuable energy resource using ionic liquid (IL)–based electrochemical systems. The employed ionic liquid, [DBUH][Im], combines the strong CO_2 affinity of imidazole with the high basicity of DBU, promoting selective carbamate formation while suppressing parasitic reactions. CO_2 chemisorption induces ion rearrangement at the electrode–electrolyte interface, generating a measurable open-circuit voltage shift. However, the high viscosity of the pristine IL significantly restricts ionic mobility, especially after CO_2 absorption. Dilution with propylene carbonate improves conductivity and enhances electrochemical performance. A multiparametric study was conducted under realistic working conditions, evaluating gas flow rate influence, CO_2/N_2 selectivity, operating temperature, and long-term stability. Moreover, the introduction of a supporting-salt further improved ionic conductivity, interfacial properties, and pore accessibility, leading to higher capacitance and harvested power. Overall, these results highlight the potential of tailored IL-based electrolytes for integrated CO_2 capture and energy conversion technologies.

1 | Introduction

In 2024, total energy-related carbon dioxide (CO_2) emissions rose by 0.8%, reaching a record high of 37.8 Gt. This increase contributed to atmospheric CO_2 concentrations hitting an all-time high of 422.5 ppm, 50% above preindustrial levels [1]. As global demand for energy continues to grow, fossil fuels are expected to remain a dominant source of energy for the coming decades; consequently, atmospheric CO_2 levels are projected to keep rising. As efforts to reduce greenhouse gas emissions have largely fallen short of their targets, the focus has increasingly shifted toward mitigating the impacts of ongoing emissions. In this context, the need to capture and manage CO_2 released from industrial and energy-related activities has become a critical component of climate strategy. Carbon capture technologies are now viewed not merely as complementary measures but as essential tools for limiting atmospheric CO_2 concentrations in the absence of sufficient emission reductions.

In parallel with carbon capture, increasing attention is devoted to CO_2 utilization and reduction technologies as integral components of a comprehensive decarbonization strategy. These approaches not only prevent further accumulation of CO_2 in the atmosphere but also offer pathways for converting CO_2 into value-added chemicals, fuels, and materials. Among the various strategies, thermochemical [2], photochemical [3–5],

Simone Martellone and Davide Molino contributed equally to this work.

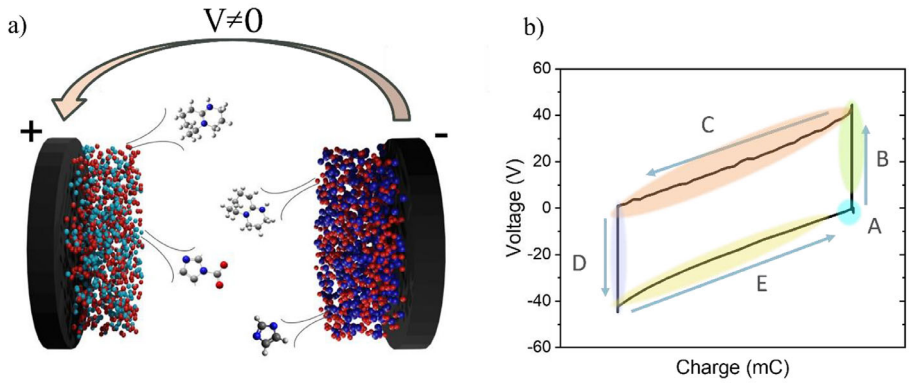

FIGURE 1 | Setup and experiment design. (a) Cell arrangement during step B, (b) the harvesting process cycle inspired to the CAPMIX procedure in voltage vs charge representation.

electrochemical [6, 7], and biological [8, 9] methods are under active development to reduce CO_2 to useful products such as carbon monoxide, formic acid, methanol, or hydrocarbons.

Despite these promising avenues, CO_2 sequestration through chemical absorption remains one of the most widely implemented techniques for carbon dioxide sequestration that relies on amine-based solvents, such as monoethanolamine (MEA). However, this technology has several critical drawbacks. The production of MEA itself is carbon intensive, since it originates from ammonia synthesized via the Haber–Bosch process [10]. Moreover, the regeneration of the solvent requires large amounts of heat that can lead to thermal degradation, generating carcinogenic nitrosamines [11].

To overcome these limitations, alternative strategies have attracted growing attention [12]. Among them, ionic liquids (ILs) stand out due to their non-volatility, structural tunability and high CO_2 absorption capacity [13], while offering opportunities for capacitive electrochemical energy storage devices to complement battery and supercapacitor technologies [14, 15]. These unique characteristics have inspired the development of various technologies aimed at designing energy storage devices capable of capturing CO_2 [16–20].

The aim of our work is to develop a technology capable of capturing carbon dioxide spontaneously, employing safe materials that also ensure long device lifetimes. By following this goal, in our previous work we exploited the interaction between an IL and CO_2 to design a supercapacitor able to selectively capturing CO_2 while simultaneously harvesting energy from the IL-CO_2 interaction [21]. The cell design and the reactions involved are reported in Figure 1a. The device and the modus operandi are deeply described in our previous work [21]. Briefly, the device is composed of two commercial gas diffusion layers (GDL 28BC, Sigracet) and a polymeric separator soaked with 100 μL of ionic liquid, which acts as an electrolyte and as a CO_2 capture medium. The IL used was pure [DBUH][Im], and CO_2 capture occurs through anions, imidazole, a chemical reaction yielding imidazole carbamate formation, while DBU's high basicity prevents its reaction with CO_2.

We observed that exposing the positive electrode to a CO_2 stream results in a spontaneous increase of the open circuit voltage for several seconds. This phenomenon can be attributed to the transient asymmetry induced in the device during the CO_2 exposure. In fact, while CO_2 is chemisorbed at the exposed side of the cell, leading to carbamate formation, the opposite side initially remains unaffected, and the anion is still present as [Im]. This asymmetry, in which [ImCOO] is present on one side of the cell and [Im] on the other, results in the observed OCV shift. The energy harvesting process was developed by exploiting this phenomenon, following the operating principle of the CapMix cycle originally proposed by Brogioli [22], which is based on a four-step process as reported in Figure 1b. In the adopted protocol, the cycle proceeds as follows: (A) the device is short-circuited for a few minutes to establish a uniform initial condition across experiments; (B) CO_2 is flushed into the device under open-circuit conditions until the voltage reaches a peak value; (C) the gas flow is stopped and the cell voltage is discharged through an external load using a constant current; (D) nitrogen (N_2) is flushed through the device to remove adsorbed CO_2 and regenerate the electrolyte. Finally, since step (D) also produces a voltage swing toward negative values, it is again possible to extract energy through a constant-current discharge (E), eventually returning to the starting point (A).

However, the high viscosity of the ionic liquid resulting from strong ion–ion interactions significantly hinders the electrochemical performance of the device. This issue gets worse after CO_2 absorption, as chemisorption induces a transition of the ionic liquid into a thicker state, severely limiting mass transfer [23]. To overcome this limitation, a low-viscosity, high-dielectric aprotic cosolvent was introduced to enhance ionic mobility. Propylene carbonate (PC) was selected for this purpose, as it increases ionic conductivity by solvating charged species and preventing ionic coupling.

To advance this technology, it is crucial to investigate key aspects that determine its practical viability. The device under study serves as a potential bridge between greenhouse gas emissions and the production of high-value CO_2-derived products, and its feasibility depends on exhibiting high selectivity for CO_2 over other gases. In real-world applications, such as flue gas streams, nitrogen (N_2) is commonly present alongside CO_2 as a major component. For instance, a 500 MW coal-fired power plant emits flue gases containing approximately 14% CO_2 and 73% N_2, while a gas-fired plant of the same capacity produces flue

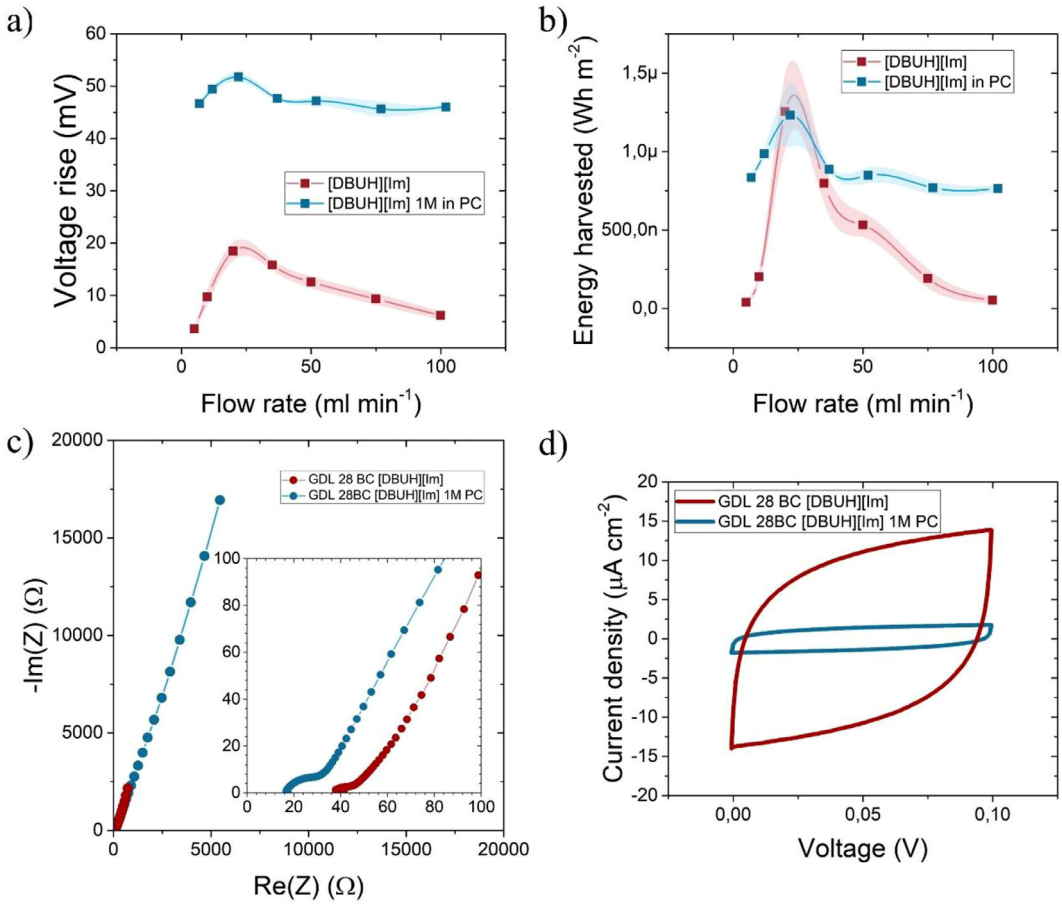

FIGURE 2 | Influence of gas flow rate in supercapacitor electrochemical performance. In (a), the recorded voltage rise as a function of the flow rates, and in (b), the measured harvested energies for the pure [DBU][Im] and [DBU][Im] 1 M in PC. The solid lines serve to guide the eye, while the area defines the error. (c) EIS (1 MHz:10 mHz). (d) Cyclic voltammetry was recorded at 5 mV s^{-1} for the [DBU][Im] and [DBU][Im] 1 M in PC.

gases with about 4% CO_2 and 76% N_2 [24]. Literature suggests that pairing imidazolium anions with superbases is a promising strategy for CO_2 capture: Zhu et al. demonstrated that the ionic liquid [DBUH][Im] exhibits strong potential for this application [25]. Moreover, it has been confirmed that [DBUH][Im] does not chemically interact with nitrogen [26], supporting its feasibility for use with flue gas mixtures. Therefore, evaluating the device performance under different CO_2 concentrations is critical to assess its real-world applicability.

Another key parameter investigated in this work is temperature. Deviations from room-temperature can significantly affect reaction kinetics, ion transport, electrolyte viscosity, and diffusion coefficients, all of which directly influence the overall performance of the device. Since practical applications often involve fluctuating thermal conditions, assessing performance under controlled temperatures is essential to evaluate operational robustness, efficiency, and stability. Temperature-dependent studies also provide critical insight into the optimal working conditions for maximizing energy storage capability.

2 | Results

In the previous work of Molino et al. [21], pure [DBUH][Im] showed efficient CO_2 capture (1 mol captured CO_2 per mole of IL), but its high viscosity (30 mPa.s) lead to low conductivity and strong interfacial dissipative behavior, not allowing for an efficient harvesting process in the CO2Cap cell. Dilution in PC allowed to reduce ion–ion interactions and self-discharge, while preserving the CO_2 sorption properties. Indeed, since PC does not absorb CO_2, a 1 M [DBUH][Im] solution in PC still achieves 0.9 mol CO_2 per mole of IL. ATR-IR spectra proved that the capture process relies only on the chemical interaction between the [Im] anion without involving PC. PC was proved to make the CO2CAP process faster, less dissipative, and energetically favorable. A drawback of this approach was a reduction of specific capacitance of the overall system, possibly due to solvent interaction with IL, compromising its ionization level. [DBUH][Im] is synthesized starting from DBU and ImH precursors, undergoing an acid-base proton exchange. In the field of protic ILs (PILs), it is affirmed that the ionization yield of this proton exchange process is strictly related to the pK_a difference (ΔpK_a) of the precursors [27]. According to available data, DBU and ImH have a tendency to show low ΔpK_a in polar solvents, suggesting that the experienced capacitance loss in the CO2CAP experiments could be addressed to this PILs chemical reaction to a chemical equilibrium were both PIL and precursors exist in the PC solution. To compensate for the capacity loss, a supporting salt ($Et_4N\ BF_4$) was added to supply additional charge as bias charge for device capacitance, while the PIL remains the functional electrolyte for the harvesting process. The resulting

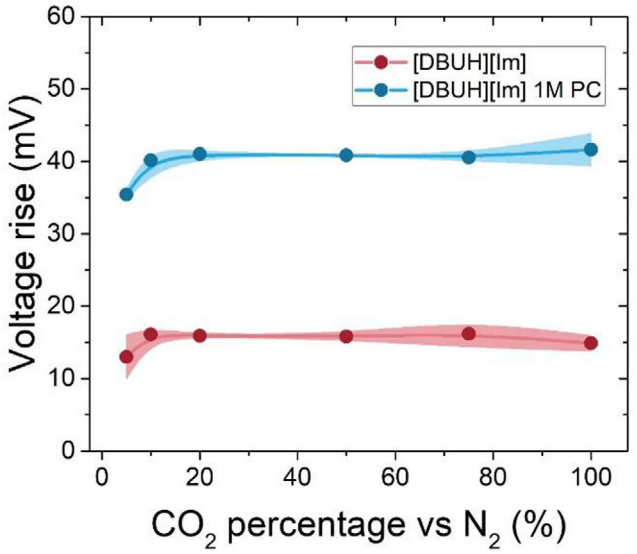

FIGURE 3 | Comparison between induced voltage rise at different CO_2 percentages by a diluted and an undiluted system. The solid lines serve to guide the eye, while the area defines the error.

electrolyte system will be investigated by NMR, rheology, and conductivity measurements, and its impact on the CO2Cap cell will be evaluated.

2.1 | On the Effects of Flow Rate, CO_2 Percentage, and Temperature

2.1.1 | CO_2 Flow Rate Effect

In the CO2CAP cell, gases flow across the positive GDL electrode and permeate through it to reach the electrolyte, enabling efficient contact with the capture media. However, excessive gas flow rates can cause electrolyte displacement and uneven distribution within the electrochemical cell, compromising cell performance.

Here, we investigate how varying flow rates can influence the performance of cells assembled with pure IL and diluted IL configurations, in terms of voltage rise and harvested energy, in order to identify optimal operating conditions. As evident from Figure 2, during CO_2 capture, the voltage rise exhibits distinct trends depending on the electrolyte state. In the case of a pristine electrolyte, the device's voltage variation is strongly influenced by the flow rate, whereas this dependence is deeply attenuated when PC is added. Notably, in both scenarios, optimal performance is observed at 20 mL/min. By comparing Figure 2a,b, it is evident that although the CO_2-induced voltage rise differs significantly between the diluted and undiluted cases, the harvested energy remains similar. This outcome is clearly related to the difference in device capacitance, as denoted by the cyclic voltammetry and electrochemical impedance spectroscopy (Figure 2c,d). The introduction of a solvent halves the equivalent series resistance of the device (Figure 2c), but reduces as well the area of the cyclic voltammetry (Figure 2d), and so of the overall capacitance, confirming the crucial role capacitance plays in the energy harvesting process.

2.1.2 | CO_2 Selectivity

While previous work focused on device performance using pure CO_2 as the inlet gas, real-world applications will involve flue gases largely composed of nitrogen. As highlighted in the introduction, the electrolyte shows low affinity for competing gases, which contributes to its high selectivity for CO_2 absorption over other gases such as nitrogen and methane. However, the presence of gases other than CO_2 has been reported to reduce CO_2 solubility and the selectivity of the system [28], potentially reducing the harvested energy. Here, we evaluate the harvested energy by varying the composition of the inlet gas, specifically analyzing CO_2/N_2 mixtures with CO_2 concentrations of 5%, 10%, 20%, 50%, 75%, and 100%. Figure 3 confirms the improvement PC introduces in the voltage rise, compared to undiluted [DBUH][Im] at 100% CO_2 concentration. Interestingly, when reducing the CO_2 amount in the incoming gas, both analyzed electrolytes do not show any behavior change, demonstrating that the cell could work properly even under low CO_2 concentrations, highlighting the strong selectivity of [DBUH][Im].

2.1.3 | Temperature Effect

Temperature strongly influences both the CO_2 solubility in ionic liquids ([DBUH][Im]) and the physicochemical properties of the ILs themselves, particularly viscosity. Between 25°C and 40°C, both the absorption capacity and rate increase with rising temperature, likely due to synergistic effects of mass transfer and reaction kinetics. However, above 45°C, the absorption capacity starts decreasing [25], owing to the exothermic nature of the gas dissolution process and the consequent weakening of intermolecular interactions between CO_2 molecules and the IL.

Temperature also affects ionic liquid viscosity, as described through Vogel-Fulcher-Tammann (VFT) quasi-empirical relations [29]. Although this model may not always perfectly reproduce the behavior [30], it is commonly reported that the viscosity of ionic liquids decreases as temperature increases (Figure S5), except in rare cases where anomalous temperature-viscosity trends are observed in certain temperature ranges [31].

This decrease in viscosity enhances the mobility of ions within the electrolyte, thereby improving mass transport processes and electrolyte penetration into the porous carbon. As a result, improved wetting increases the accessible surface area for electrochemical interactions, which, combined with reduced resistive behavior, leads to higher device capacitance, as shown by the larger CV areas at higher temperatures (Figure S5c,e). In Electrochemical Impedance Spectroscopy (EIS) of electric double-layer capacitors, the semicircle in the high-frequency region of the Nyquist plot reflects interfacial resistances (contact resistance, electrode resistance, and electrode/electrolyte interface resistance). With increasing temperature, reduced resistive behavior shifts this region toward lower real impedance values, indicating improved device performance (Figure S5b,d).

Therefore, although higher temperatures may compromise CO_2 capture efficiency due to reduced solubility, they

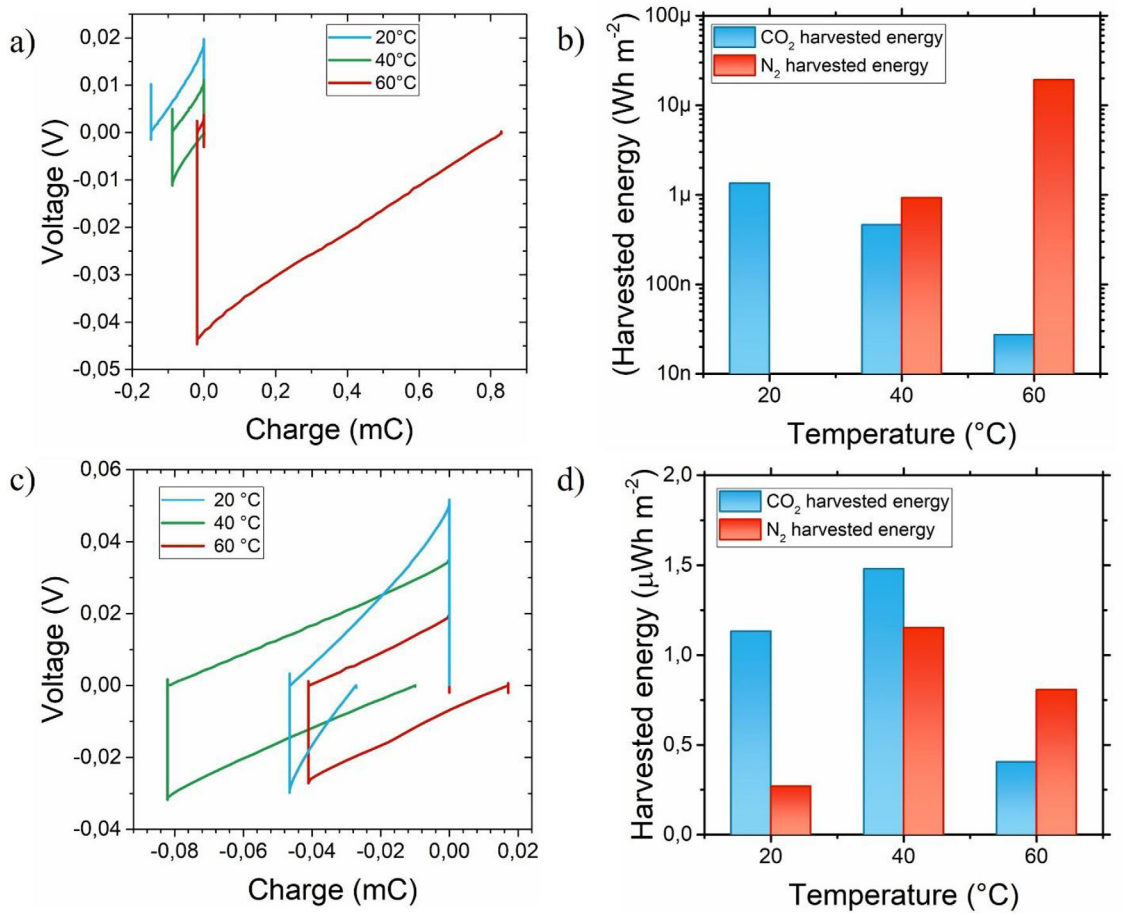

FIGURE 4 | Temperature effect on supercapacitor electrochemical performances. (a) Voltage vs charge plot and (b) extracted energy of pure electrolyte device at different operating temperatures, (c,d) same plots for the diluted case.

simultaneously benefit the overall performance of electrochemical systems by enhancing ionic conductivity and improving electrode–electrolyte interfacial properties. These considerations remain valid for both devices; the solvated ionic liquid does not exhibit different behavior.

The results of the energy harvesting cycles are reported in Figure 4. In the case of the pure electrolyte device, a decrease in the energy extracted during CO_2 capture is observed. This reduction is clearly due to the shrinkage of the carbon dioxide-induced voltage rise, which drops from about 20 mV to less than 5 mV (Figure 4a,b). This behavior can be attributed to the reduced solubility of carbon dioxide in ionic liquids as the temperature increases. At the same time, the voltage swing induced by nitrogen-stimulated regeneration increases progressively. This phenomenon may be related to the temperature-induced CO_2 release, which enhances this voltage swing (Figure 4c,d). Conversely, for the diluted electrolyte case, the highest extracted energy is observed at 40°C. At this temperature, both the energy extracted from the carbon dioxide capture and that from its release under nitrogen reach their maximum values. This occurs even though a higher temperature negatively affects the voltage rise. In this case, however, the increase of device's capacitance compensates for the reduction in the voltage swing. Indeed, at 40°C, the capacitance of the diluted system increases by a factor of 2.8 compared to RT case, while for the undiluted system, the increase is limited to a factor of 1.7. Considering the voltage swing, on the other hand, this is 1.4 times reduced for the diluted case and 1.7 times for the undiluted case.

2.2 | Effect of Supporting Salt

A possible strategy to increase the harvesting performance of the cell is to act on its electrolyte composition, with the goal of tuning the CO_2 harvesting device transport and interfacial properties without introducing additional CO_2-reactive chemistry. To do so, we decided to test a mixture of [DBUH][Im] (to maintain the CO_2 adsorption properties required by the CO2Cap process) and Et_4N BF_4 (for its highly conductivity and wide use as an electrolyte for supercapacitor applications [32]). To assess the inertness of Et_4NBF_4 in PC, some control measurements (Figures S2 and S6) were carried out, confirming that it does not contribute to CO_2 uptake, showing negligible mass variation and voltage rise under CO_2 exposure.

From a rheological perspective, mapping viscosity across the [DBUH][Im]/Et_4NBF_4/PC composition space shows that increasing the total ionic content increases viscosity, with the highest viscosity region occurring around equimolar 1 M [DBUH][Im] / 1 M Et_4NBF_4, as evidenced in Figure 5. Importantly, this maximum remains well below the viscosity of the neat ionic liquid

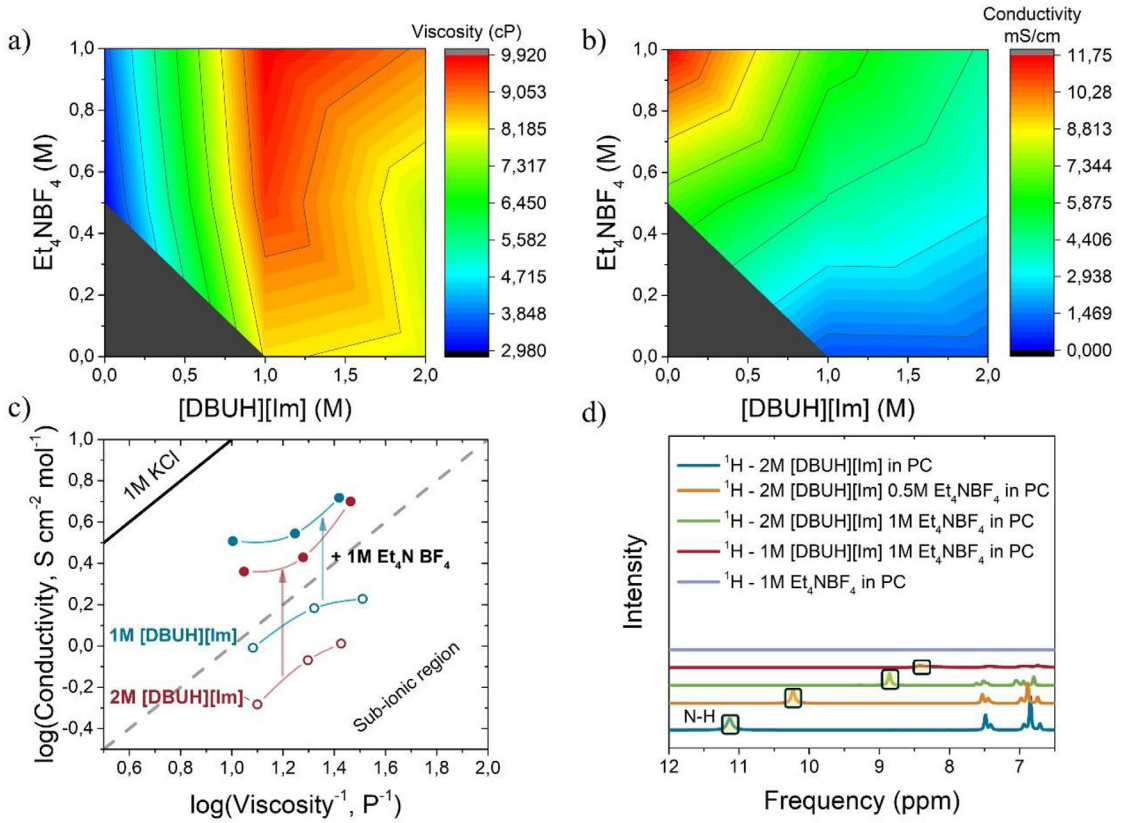

FIGURE 5 | Preliminary analysis on supporting salt + ionic liquid electrolyte. Viscosity (a) and conductivity (b) of solutions containing [HDBU][Im] and Et_4N BF_4 in PC according to what is reported on the axes. (c) Walden plot (i.e., molar conductivity vs fluidity) of some notable compositions. (d) Chemical shift of the N-H peak induced by the variation of the Et_4N BF_4 amount.

TABLE 1 | Walden table.

Electrolyte	Slope	Intercept	Conductivity activation energy (kJ mol^{-1})	Viscosity activation energy (kJ mol^{-1})
2 M [DBUH][Im]	0.93	−1.31	13.9	−15.3
1 M [DBUH][Im]	0.57	−0.62	11.2	−20.0
2 M [DBUH][Im] + Et_4NBF_4	0.81	−0.54	15.6	−19.4
1 M [DBUH][Im] + Et_4NBF_4	0.49	−0,01	9.4	−19.1

previously reported, confirming that dilution in PC strongly reduces viscosity relative to the bare PIL. The same qualitative trend persists at 40°C and 60°C, where viscosities drop overall due to the temperature effect, but preserve the composition dependence (Figure S3). Conductivity measurements across the same composition window show complementary behavior: the highest conductivity is observed for 1 M Et_4NBF_4 in PC (no IL), while increasing the fraction of [DBUH][Im] reduces conductivity because the PIL is intrinsically less conductive than the supporting salt under comparable conditions (Figure 5). Still, adding Et_4NBF_4 to IL-containing mixtures produces a strong conductivity gain at a fixed IL concentration, which is the practical motivation for introducing the supporting electrolyte.

Combining conductivity and viscosity allows construction of a Walden plot at {20, 40, 60} °C (i.e., molar conductivity vs. fluidity, Figure 5c). Adding Et_4NBF_4 shifts the electrolyte behavior toward a more ionic one, i.e., closer to the ideal reference line (usually diluted KCl) and away from the sub-ionic regime, as evinced from Figure 5c. This is consistent with an increase in effective charge transport at a given viscosity. According to the analysis of the Walden data (Table 1), the slopes (E_σ/E_η) are always less than one, implying that the transport mechanism is mainly limited by the viscous drag, especially at low PIL content. This is further proved by analyzing the sole activation energies.

However, the Walden plot reflects bulk electrolyte behavior, not the specific dissociation of a single ion pair. In our electrolytic multi-ion system (DBUH+, Im-, Et_4N+, BF_4-), an apparent "increase in ionicity" cannot be uniquely assigned to increased dissociation of the PIL pair, but the Walden shift could largely arise from the highly dissociated Et_4NBF_4 in PC, boosting the

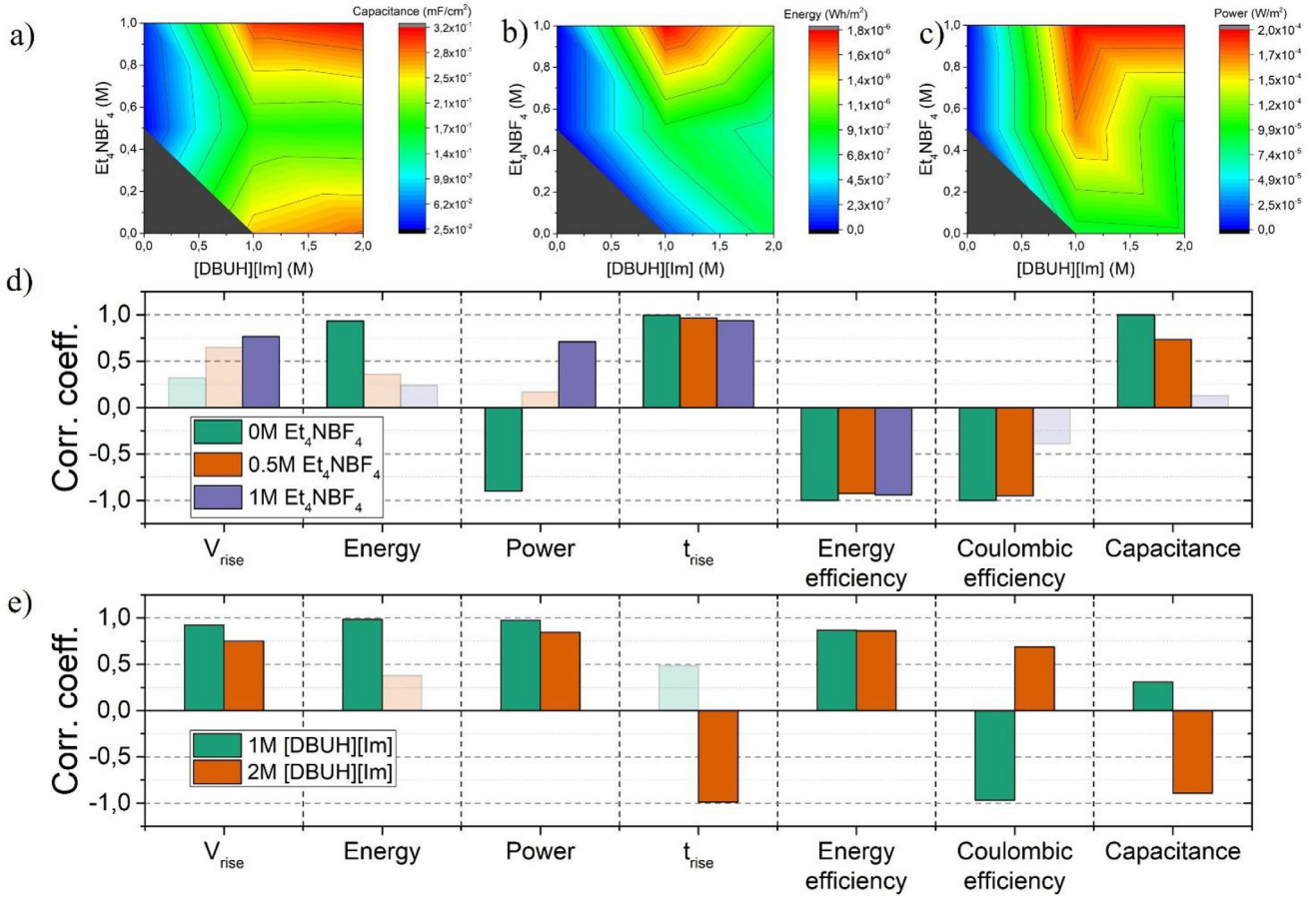

FIGURE 6 | Multiparametric study on supporting electrolyte–ionic liquid device. Respectively maps of the capacitance (a), energy (b), and power extraction (c) of the supercapacitor used to harvest energy from carbon dioxide capture with respect to the composition of the electrolyte in terms of ionic liquid–supporting salt concentration. Capacitance is extracted from CV at 100 mV with 5 mV s^{-1} scan rate, energy and power are computed from the CO2Cap extraction cycle. (d) Representation of the correlation coefficients between several different figures of merit and concentration of supporting salt at fixed [HDBU][Im] and (e) concentration of [HDBU][Im] at fixed concentration of Et_4NBF_4. Shadowed columns present a p-value > 0.05.

overall conductivity. Thus, the Walden plot shift can be interpreted phenomenologically: supporting salt makes the electrolyte behave more like a well-dissociated conductor at the same viscosity, which is beneficial for capacitive mixing.

NMR analyses (Figure 5d) were exploited to address the overall electrolyte content. The 1H NMR series included in the SI shows two robust trends for the DBUH-associated N-H resonance: systematic chemical-shift changes of the N-H signal with increasing Et_4NBF_4 (e.g., from 11.14 ppm in 2 M [DBUH][Im] to 8.86 ppm in mixed conditions), and a strongly perturbed/broadened situation near equimolar conditions and strong broadening and loss of peak intensity at higher salt concentration, up to the point where the N-H resonance vanishes. These spectral changes should be described primarily as a salt effect: adding Et_4NBF_4 changes the local electronic environment and solvation structure around the DBUH-containing species through well-known mechanisms (ionic-strength-driven deshielding/shielding trends depending on the microenvironment, dynamic ion pairing, and rearranged PC solvation), and it can accelerate exchange processes. Therefore, the N-H signal becomes broader and less intense due to faster exchange/clustering and relaxation effects proper of unaltered PIL activity. Consequently, Walden shift toward the ionic region, at modestly changed viscosity, charge transport becomes less hindered, consistent with screening of Coulombic interactions and/or reduced association phenomena in the presence of added supporting electrolyte and PC dilution. NMR salt-effect signatures (chemical-shift changes and broadening) independently indicate that the local solvation/association landscape around DBUH-containing species is being reorganized by Et_4NBF_4 and by increased ionic strength. Thus, the supporting salt does not merely "add carriers" but also modifies microstructure and PIL exchange dynamics. This is the kind of microscopic change that can reduce strongly paired structures ([DBUH]…[Im]) and improve macroscopic conductivity without requiring a large shift in acid-base speciation.

In Figure 6, we report the electrochemical performance. The optimum behavior at 1 M/1 M reflects a transport plus interface optimum (conductivity/ESR and pore access/double-layer packing), while NMR confirms that this composition produces a strong salt-induced reorganization of the local environment [27, 33–37].

The highest capacitance is observed in the bottom right corner (0 M Et_4NBF_4 and 2 M [DBUH][Im], 0,28 mF cm^{-2}) and in the top

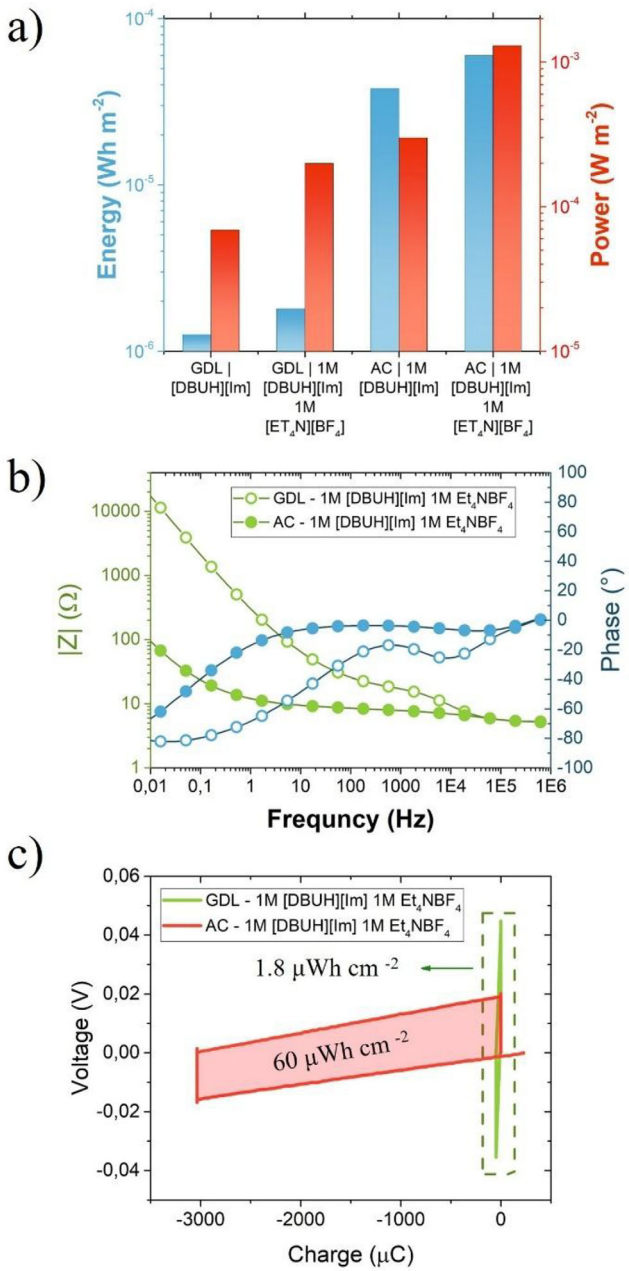

FIGURE 7 | Effects of the addition of activated carbon slurry on the surface of the electrode. (a) Comparison of energy and power extracted from the energy harvesting process. In both graphs, data related to GDL | [DBUH][Im] and GDL | [DBUH][Im] 20wt.% in [EMIM][Ac] come from a previous publication [21], (b) Bode plot of the comparison between a device with pure electrolyte and a device with the introduction of the supporting salt, (c) energy extraction cycles of GDL and activated carbon devices.

center (1 M Et_4NBF_4 and 1 M [DBUH][Im], 0,3 mF cm^{-2}), while at 1:2 and 1:4 salt-IL ratios, the capacitance is about 45% lower.

Energy harvesting performances (Figure 6b,c), show a maximum extracted energy of 1.8 µWh m^{-2} at equimolar concentration of salt and ionic liquid In fact, at 1 M [DBUH][Im] 1 M Et_4N BF_4, the extracted energy is comparable with the best performing electrolyte composition with bare GDL (Figure 7e,f of [21]), however the generated power doubles from 0.1⁻ to 0.2 mW m^{-2}.

This improvement can be attributed to the increase in capacitance produced by the supporting salt, which increases the number of available ions, preventing the drawbacks of ion pairing visible at higher concentrations. The investigated IL is a protic ionic liquid (PIL), formed through proton transfer between a Brønsted acid and a Brønsted base. As pointed out by Yoshizawa et al. [33], the driving force for proton transfer can be approximated by the difference in pKa values of the acid and the base. When ΔpKa > 10, a complete proton transfer is expected, leading to full ionization. In [DBUH][Im] case ΔpKa ≈ 2, suggesting the coexistence of ionic and neutral species in equilibrium [34].

To analyze how ionic liquid and supporting salt affect the performance of the cell, we studied correlations between electrolyte composition and voltage rise (V_{rise}), harvested energy (E), discharged power (P), CO_2-induced rising time (t_{rise}), energy efficiency (η_E), coulombic efficiency (η_C), and capacitance (C). This study evaluates the degree of relationship between two different independent variables, exploiting the Pearson model. The output of this method, exploited at this first stage, is the correlation coefficient and the p-value. The first parameter can assume a value comprised between −1 and +1. The closer to 0, the lower the correlation, while the sign indicates if the correlation is direct or inverse. The p-value represents the reliability of the correlation: in general, a correlation is accepted if the p-value is smaller than 0.05. Results are summarized in Table 2.

The ionic liquid shows some strong correlations with the voltage rise caused by CO_2 absorption, the voltage rising time, and an inverse correlation with energy efficiency (evaluated from cyclic voltammetry). These relationships can be ascribed to the system's nature itself: voltage rise can be related to a Nernstian contribution of the potential variation at the anode where the gas is fluxed, as already proved in a recent work [35]. Similarly, the rising time is directly correlated, meaning that the PIL concentration at the interface plays a potential role in defining the overall process frequency, therefore, the overall harvesting cycle power. Concerning the reduced energy efficiency, the overall PIL electrochemical stability and response at the GDL interface (see [21]) the concentrated the IL in the electrolyte phase, the lower will be the energy efficiency and thus the overall harvesting yield.

On the other hand, supporting salt presents only moderate correlations with the harvested energy, generated power, and energy efficiency. From here, some hints can be obtained to design an electrolyte in a proper way. It is possible to state that adding ET_4N BF_4 has no detrimental effect is produced but it slightly improves some properties of the system. Otherwise, increasing [DBUH][Im] produces an improvement on CO_2-induced voltage rise, but reduces energy efficiency and extends the rising time.

It is possible to go deeper with the analysis by considering the correlation coefficients of [DBUH][Im] at one fixed concentration of Et_4NBF_4 (Figure 6d) and vice versa (Figure 6e). The correlations for those plots are in general stronger and more reliable, if compared to the general case. However, for some parameters, the correlation coefficient is affected by the concentration of the fixed electrolyte. In Figure 6d, the correlation coefficient of power is strongly negative (−0.9) for 0 M ET_4N BF_4 and moderately

TABLE 2 | Pearson correlation factors for all the datasets. Red values are the one presenting a p-value > 0.05.

	V_{rise}	E	P	t_{rise}	η_E	η_C	C
[HDBU][Im]	0.64	0.26	0.28	0.75	−0.80	−0.62	−0.36
$ET_4N\ BF_4$	0.06	0.54	0.43	−0.33	0.56	−0.20	−0.30

positive for 1 M $ET_4N\ BF_4$ (0.71). By crossing these results with the one in Figure 6e, it is possible to appreciate how the correlation coefficients of the power at different [DBUH][Im] concentrations remain almost constant. This behavior suggests that ET_4N acts as the primary variable in controlling the power regime, while DBU acts as a secondary factor whose effect is modulated by the ET_4N concentration. Following the same thought process, it is possible to affirm that for coulombic efficiency and capacitance, the primary variable is the [DBUH][Im] concentration. This, in principle, could also be applied to the t rise parameter, however, for the 1 M [DBUH][Im] case, the p-value is > 0.05, making the correlation coefficient not reliable.

A direct comparison between the IL and the system with supporting salt is available in Figure 7. This improvement is related to the reduction of the equivalent series resistance (from about 20 Ω to about 5 Ω), combined with the improvement of the capacitance (from 0.26 mF cm^{-2} up to 0.3 mF cm^{-2}). Moreover, the introduction of 1 M of $Et_4N\ BF_4$ to 1 M [DBUH][Im] provides a reduction of the resistance also at the low frequencies, moving from about 5 kΩ to about 2.5 kΩ (Figure 2a)) This allows for the discharge of the supercapacitor, avoiding all the ohmic losses due to a higher impedance, allowing to reach higher power.

To complete the discussion for what deals with the introduction of a supporting salt, it was decided to test at the best electrolyte composition an activated carbon electrode. This was done to improve as much as possible, the capacitance of the device by acting on the active surface of the electrodes. Comparing impedance spectroscopy in Bode representation, it is possible to appreciate how at high frequencies, the ESR is unvaried by the introduction of the activated carbons, while at low frequencies the modulus of the impedance is highly reduced, meaning an increase in the capacitance. This increase was confirmed by the analysis of the cyclic voltammetry. In Figure S12b, the CV of GDL and GDL+AC electrodes are reported: the capacitance increases from 0.3 mF cm^{-2} up to 35 mF cm^{-2}. Those improvements allow to reach an extracted energy of 60 μWh m^{-2} and a power output of 1 mW m^{-2}. As shown in Figure 7a, these results outperformed those obtained in the previous publication [21].

2.2.1 | Lifetime

The ability to perform consecutive cycles is enabled by the regeneration step, during which an N_2 flush breaks the chemical bonds between imidazole and carbon dioxide, effectively restoring the device. This desorption process takes longer than the absorption phase due to a re-adsorption mechanism: once a CO_2-imidazole bond is broken, the released CO_2 molecule can interact with neighboring imidazoles, temporarily rebinding before complete removal. The duration of this phase is determined empirically to ensure cycle repeatability. In order to prove that the regeneration time is sufficient for reliable cell performance, we alternated CO_2 and N_2 flushes while monitoring voltage variations as reported in Figure 8; the data confirm that the potential shifts remain consistent over more than 1000 cycles.

It was decided to compare the cycling performance of a device using pure [DBUH][Im] as the electrolyte with that of a device employing a 1 M [DBUH][Im] and 1 M Et_4NBF_4 solution in propylene carbonate. Both devices show strong long-term stability, with ΔV remaining consistent after each CO_2-N_2 cycle. The diluted electrolyte exhibits larger and faster voltage variations because of its lower resistance and viscosity, which also facilitate CO_2 desorption and consequently shortens the regeneration step. As a result, the diluted device completes 1200 cycles in approximately 100 h, whereas the pure [DBUH][Im] cell takes 400 h to reach 1000 cycles.

The ageing behavior of the mixtures of ionic liquid/supporting salt was evaluated by comparing the impedance spectroscopies of the freshly prepared solutions and the 6-month-aged ones. As reported in Figure 8c, for high-concentration solutions (2 M [DBUH][Im] with 1 M or 0.5 M Et_4NBF_4), ageing results in a shift of the impedance toward higher resistive values, with the real-axis intercept rising from 160–300 Ω to 700 Ω. Conversely, for the selected optimal composition (1 M [HDBU][Im] 1 M $ET_4N\ FB_4$), the increase is much smaller, passing from about 160 Ω to about 210 Ω. This result proves that the chosen concentration provides good stability against ageing. It also highlights the steady-state ageing behavior of these electrolytes, suggesting that, as a best practice, the electrolyte should be freshly synthesized whenever needed, avoiding prolonged storage.

3 | Discussion

This work reports the effects of CO_2 flow rate, gas composition, temperature, and supporting electrolyte to the recently developed CO2CAP harvesting cell. Indeed, a broad and systematic evaluation of energy harvesting devices based on CO_2 chemisorption in functionalized ionic liquids is reported, delivering insights that are critical for their future technological translation. Using [DBUH][Im] as a benchmark electrolyte, we demonstrate that a simple yet powerful concept (i.e., the interfacial voltage shift induced by CO_2 binding) can be exploited to generate usable electrical energy. However, this fundamental mechanism is strongly shaped by the physicochemical properties of the electrolyte, which can either enable or hinder device operation.

The first key outcome is the identification of ionic mobility as a central parameter. While neat [DBUH][Im] provides high selectivity for CO_2 capture, its excessive viscosity reduces ionic conductivity and limits the energy harvesting performance. Dilution with propylene carbonate emerges as an effective strategy to

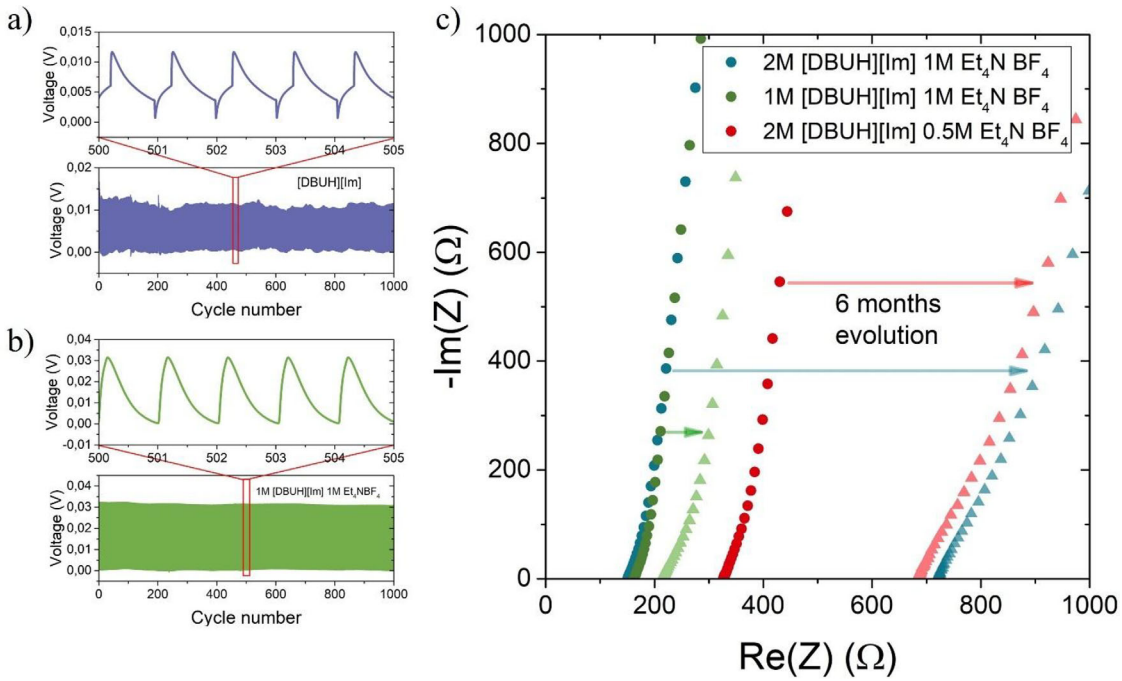

FIGURE 8 | Log-time evolution of performances. (a) Life cyclability of a GDL|[DBUH][Im] |GDL device, (b) life cyclability of a GDL|1M[DBUH][Im] 1 M Et_4N BF_4|GDL device, (c) evolution of the impedance spectroscopy of high concentration ionic liquid + supporting salt mixtures after 6 months.

stabilize the overall performance of the device and overcome the aforementioned challenges: it attenuates ion pairing, makes the device less sensitive to external parameter variations, accelerates interfacial dynamics, and improves cycle speed, while maintaining comparable harvested energy. This finding underscores the importance of electrolyte engineering to balance CO_2 affinity with transport properties.

Another crucial aspect is selectivity under realistic conditions. We have demonstrated that [DBUH][Im] maintains nearly constant harvested energy even at very low CO_2 concentrations (5% in CO_2/ N_2 mixtures). This is a decisive step toward practical deployment, as it proves that flue gas streams from industrial plants can directly serve as feedstocks for CO_2-to-energy conversion. In addition, the system exhibits outstanding operational durability, sustaining more than 1000 consecutive absorption–desorption cycles with minimal performance degradation. Such resilience is indispensable for long-term operation in industrial environments.

Additionally, temperature effects introduce an interesting trade-off between solubility and transport. While increasing temperature reduces the extent of CO_2 capture, it simultaneously boosts capacitance and conductivity by lowering viscosity and ion pairing. For the diluted electrolyte, this balance results in optimal performance at 40°C, a temperature compatible with many industrial exhaust conditions. This opens the possibility of tuning device operation according to the specific thermal profile of a given emission source.

Finally, the integration of a supporting salt (Et_4N BF_4) in PC-based mixtures reveals a powerful route for performance enhancement. By improving ionic conductivity and pore accessibility, the supporting salt dramatically reduces interfacial resistance and boosts both capacitance and power density. With optimized compositions and activated carbon electrodes, the system achieves energy and power metrics that significantly surpass previous benchmarks, establishing a new performance level for CO_2 electrochemical harvesting devices.

In conclusion, this study confirms ionic liquid–based electrochemical systems as a promising route to turn CO_2 emissions into a usable energy resource. By dissecting the interplay between chemistry, transport, and device operation, we provide both fundamental understanding and practical guidelines that will inform the next generation of CO_2 capture and conversion technologies.

4 | Materials and Methods

4.1 | Materials

Propylene carbonate (PC) and Tetraethylammonium tetrafluoroborate (Et_4NBF_4) were purchased from Merck-Sigma-Aldrich. The gas diffusion layer (GDL) was 28BC provided by Sigracet. For the synthesis of the ionic liquid, 1,8-diazabicyclo-undec-7-ene (98%), imidazole (99%), and methanol (98%) purchased from Sigma–Aldrich were used. 1,8-Diazabicyclo[5.4.0]undecane imidazolide ([DBUH][Im]) was prepared by slightly modifying a reaction described in the literature [21]. A 50% (w/w) solution of 1,8-diazabicyclo-undec-7-ene in methanol was neutralized using an equimolar amount of imidazole. After the reaction, the methanol was evaporated using a rotary evaporator, and the IL was dried at 60°C for 24 h prior to use in a vacuum oven with a vacuum level below 133 Pa.

To increase the overall capacitance of the device, in some configurations, it was decided to add on top of GDL a carbon

slurry produced by mixing together in a water-based solution an amount of 85wt.% activated carbons (YP–50 F from Kuraray), 10wt.% carbon black (Timical Super C65 from Imerys), and 5wt.% sodium carboxymethyl cellulose (from MTI, average Mw 400 000).

In order to define the optimal ratio between the ionic liquid and the supporting salt, a 3 × 3 matrix was designed by varying the concentration of the $Et_4N\ BF_4$ and [DBUH][Im]. In particular, the concentrations analyzed were 0, 0.5, 1 M for $Et_4N\ BF_4$ and 0 M, 1 and 2 M for [DBUH][Im]. These values were chosen considering the solubility limit of the salt (which is indeed close to its solubility limit [36]) and the optimal [HDBU][Im] concentration reported in our previous work [21]. All concentrations are referred to the final solution volume: e.g., 1 L of 1 M [DBUH][Im] – 1 M $Et_4N\ BF_4$ solution contains 1 mol of ionic liquid and 1 mol of supporting salt. To obtain a correct dispersion of $Et_4N\ BF_4$, it was decided to dissolve both salts in PC. This decision comes from the already tested good compatibility of [DBUH][Im] with PC, while in the literature, previous works report the use of $Et_4N\ BF_4$ salt in PC solvent for EDLC supercapacitor applications [32, 37–40].

4.2 | Physical-Chemical Characterizations

Rheology measurements were performed in a parallel disk rheometer MCR 302, manufactured by Anton Paar, exploiting a 25 mm diameter parallel disk configuration, with a distance between the plates equal to 0.6 mm. Shear rate varied from 10^- to 1000 s^{-1}, studied at 20°C, 40°C and 60°C. The temperature was controlled through the internal Peltier system, and before each temperature point, the system was let thermalize for 10 min. Reported viscosity values correspond to the average over the applied shear-rate range, since the samples exhibited a constant response within the investigated interval.

The ^{1}H-NMR and ^{13}C-NMR spectra were recorded on a Magritek Spinsolve 80 MHz spectrometer at 25°C, using 500 µL of solution for each sample.

The CO_2 absorption capacity of ILs and solutions was determined using gravimetric absorption. The sample was insufflated with CO_2, and the weight increase was recorded as a function of time until a constant weight.

4.3 | Electrochemical Measurements

Electrochemical measurements were performed using a VMP-3 system (Biologic), which includes potentiostat/galvanostat modules and frequency response analyzers for conducting electrochemical impedance spectroscopy (EIS). The EIS experiments spanned a frequency range from 10^6 to 10^{-2} Hz, with data collected at ten points per frequency decade and an applied signal amplitude of 5 mV. Open-circuit voltage (OCV) readings were also taken to monitor the cell's behavior during gas absorption, with a voltage resolution of 1 mV. Galvanostatic charge–discharge measurements were conducted at 1 mA cm^{-2} (if not otherwise mentioned) to evaluate the harvested energy and power. Cyclic voltammetries were performed at the scan rate of 5 mV s^{-1} to investigate cell capacitances prior to any experiment. Cyclability tests were conducted by alternatively flushing in the tested cell with carbon dioxide and nitrogen. Adopted flows and times are comparable to those adopted for the CO2Cap cycles (refer to the specific section). All tests were carried out using a commercially available ECC-Air test cell (El Cell GmbH), specifically designed for electrochemical studies and allowing controlled gas flow into the sample chamber.

The gas stream is regulated using two mass flow meters (EL Flow, Bronkhorst), which control the rate of CO_2 and N_2 in the outgoing flow. In the case of CO_2 flow rate tests, the flow rate was regulated at different values (5, 10, 20, 35, 50, 75, 100 mL/min). Gases were mixed according to the following procedure: the total gas flow was set at 40 mL/min, while individual flow meters were set to obtain the desired CO_2 percentage (e.g., 20% CO_2 means 8 mL/min of CO_2, 32 mL/min N_2). The gas streams were then combined using a T-shaped connector. After allowing the system to stabilize to ensure homogeneity of the gas mixture, the outlet of the T-junction was used as the gas source for the electrochemical cell. For the schematic and picture of the setup, refer to (Figure S1).

Experiments requiring a working temperature different from room-temperature were carried out using a Memmert UN30/1060 drying oven, which allows precise temperature control during electrochemical measurements.

Conductivity measurements were carried out using a standard glass conductivity cell from AMEL, with two symmetric platinum electrodes (cell constant provided by the producer K = 1).

Author Contributions

A.L. supervised and guided the project. A.L., S.M., D.M., and P.Z. conceived and designed the research. S.M. and D.M. carried out electrode fabrication, device assembly, electrochemical testing, and data analysis. S.D.M. performed the NMR experiments and analyzed the corresponding data. G.F. and S.B. synthesized the ionic liquid. S.M., D.M., and P.Z. drafted the manuscript. All authors reviewed, revised, and approved the final version of the manuscript.

Acknowledgements

This result is part of a project that has received funding from the European Research Council (ERC) under the European Union's ERC Starting Grant agreement "CO2CAP" No. 949916. This manuscript reflects only the authors' views and opinions, neither the European Union nor the European Commission can be considered responsible for them.

Conflicts of Interest

The authors declare no conflicts of interest.

Data Availability Statement

The data that support the findings of this study are available from the corresponding author upon reasonable request.

References

1. International Energy Agency, "Global Energy Review 2025 – CO_2 Emissions," 2025.

2. E. P. Komarala, A. A. Alkhoori, X. Zhang, H. M. Cheng, and K. Polychronopoulou, "Design and Synthesis of Thermally Stable Single Atom Catalysts for Thermochemical CO_2 Reduction," *Journal of Energy Chemistry* 86 (2023): 246–262, https://doi.org/10.1016/j.jechem.2023.07.032.

3. M. Zoli, D. Roldán, H. Guzmán, et al., "Facile and Scalable Synthesis of Cu_2O-SnO_2 Catalyst for the Photoelectrochemical CO_2 Conversion," *Catalysis Today* 413 (2023): 113985, https://doi.org/10.1016/j.cattod.2022.12.016.

4. M. Zoli, H. Guzmán, A. Sacco, N. Russo, and S. Hernández, "Cu_2O/SnO_2 Heterostructures: Role of the Synthesis Procedure on PEC CO_2 Conversion," *Materials* 16 (2023): 4497, https://doi.org/10.3390/ma16134497.

5. G. Cuatto, M. Zoli, M. Gallone, H. Guzmán, M. Castellino, and S. Hernández, "Standardization of Cu_2O Nanocubes Synthesis: Role of Precipitation Process Parameters on Physico-Chemical and Photo-Electrocatalytic Properties," *Chemical Engineering Research and Design* 199 (2023): 384–398, https://doi.org/10.1016/j.cherd.2023.09.047.

6. F. Zammillo, H. Guzmán, D. Polino, et al., "Assessing the Activity and Stability of Cu_2O/SnO_2-Based Gas Diffusion Electrodes for the CO_2 Conversion in Different Electrolytes: Bicarbonate vs. Ionic Liquid/Acetonitrile," *Chemical Engineering Journal* 514 (2025): 163265, https://doi.org/10.1016/j.cej.2025.163265.

7. R. Guan, L. Sheng, C. Li, et al., "Mechanochemical Carbon Dioxide Capture and Conversion," *Nature Nanotechnology* 20 (2025): 1247–1253, https://doi.org/10.1038/s41565-025-01949-6.

8. L. Tarraran, V. Agostino, N. S. Vasile, et al., "High-Pressure Fermentation of CO_2 and H_2 by a Modified Acetobacterium Woodii," *Journal of CO2 Utilization* 76 (2023): 102583, https://doi.org/10.1016/j.jcou.2023.102583.

9. G. Antonicelli, L. Ricci, L. Tarraran, et al., "Expanding the Product Portfolio of Carbon Dioxide and Hydrogen-Based Gas Fermentation with an Evolved Strain of Clostridium Carboxidivorans," *Bioresource Technology* 387 (2023): 129689, https://doi.org/10.1016/j.biortech.2023.129689.

10. P. Luis, "Use of Monoethanolamine (MEA) for CO_2 Capture in a Global Scenario: Consequences and Alternatives," *Desalination* 380 (2016): 93–99, https://doi.org/10.1016/j.desal.2015.08.004.

11. N. A. Fine, M. J. Goldman, and G. T. Rochelle, "Nitrosamine Formation in Amine Scrubbing at Desorber Temperatures," *Environmental Science & Technology* 48 (2014): 8777–8783, https://doi.org/10.1021/es501484w.

12. H. Bouaboula, Y. Belmabkhout, and A. Zaabout, "Life Cycle Assessment of Electrochemical pH-Swing Direct Air Capture," *Energy Conversion and Management* 342 (2025): 120134, https://doi.org/10.1016/j.enconman.2025.120134.

13. M. Yousefe, K. Glińska, M. Sweeney, L. Moura, M. Swadźba-Kwaśny, and A. Puga, "CO_2 Capture by Carboxylate Ionic Liquids: Fine-Tuning the Performance by Altering Hydrogen Bonding Motifs," *RSC Sustainability* 3 (2025): 2952–2961, https://doi.org/10.1039/D5SU00108K.

14. J. Xiao, H. Zhan, X. Wang, et al., "Electrolyte Gating in Graphene-Based Supercapacitors and its Use for Probing Nanoconfined Charging Dynamics," *Nature Nanotechnology* 15 (2020): 683–689, https://doi.org/10.1038/s41565-020-0704-7.

15. C. Merlet, B. Rotenberg, P. A. Madden, et al., "On the Molecular Origin of Supercapacitance in Nanoporous Carbon Electrodes," *Nature Materials* 11 (2012): 306–310, https://doi.org/10.1038/nmat3260.

16. P. Zhu, Z. Y. Wu, A. Elgazzar, et al., "Continuous Carbon Capture in an Electrochemical Solid-Electrolyte Reactor," *Nature* 618 (2023): 959–966, https://doi.org/10.1038/s41586-023-06060-1.

17. Z. Xu, G. Mapstone, Z. Coady, et al., "Enhancing Electrochemical Carbon Dioxide Capture With Supercapacitors," *Nature Communications* 15 (2024): 7851, https://doi.org/10.1038/s41467-024-52219-3.

18. Z. Xu, X. Liu, G. Mapstone, et al., "Breaking Supercapacitor Symmetry Enhances Electrochemical Carbon Dioxide Capture," *Journal of the American Chemical Society* 147 (2025): 16189–16197, https://doi.org/10.1021/jacs.5c00999.

19. S. Jin, M. Wu, R. G. Gordon, M. J. Aziz, and D. G. Kwabi, "pH Swing Cycle for CO_2 Capture Electrochemically Driven Through Proton-Coupled Electron Transfer," *Energy & Environmental Science* 13 (2020): 3706–3722, https://doi.org/10.1039/D0EE01834A.

20. Y. Jing, K. Amini, D. Xi, et al., "Electrochemically Induced CO_2 Capture Enabled by Aqueous Quinone Flow Chemistry," *ACS Energy Letters* 9 (2024): 3526–3535, https://doi.org/10.1021/acsenergylett.4c01235.

21. D. Molino, F. Raffone, P. Zaccagnini, et al., "Energy Harvesting from CO_2 Emission Exploiting Ionic Liquid-Based Electrochemical Capacitor," *Advanced Energy and Sustainability Research* 6 (2025): 2500019, https://doi.org/10.1002/aesr.202500019.

22. D. Brogioli, R. Ziano, R. A. Rica, et al., "Exploiting the Spontaneous Potential of the Electrodes Used in the Capacitive Mixing Technique for the Extraction of Energy From Salinity Difference," *Energy & Environmental Science* 5 (2012): 9870–9880, https://doi.org/10.1039/c2ee23036d.

23. H. Yan, L. Zhao, Y. Bai, et al., "Superbase Ionic Liquid-Based Deep Eutectic Solvents for Improving CO_2 Absorption," *ACS Sustainable Chemistry & Engineering* 8 (2020): 2523–2530, https://doi.org/10.1021/acssuschemeng.9b07128.

24. U. Arachchige, M. Mohsin, and M. C. Melaan, "Optimization of Post Combustion Carbon Capture Process-Solvent Selection," *International Journal of Energy and Environment* 3 (2012): 861–870.

25. X. Zhu, M. Song, and Y. Xu, "DBU-Based Protic Ionic Liquids for CO_2 Capture," *ACS Sustainable Chemistry & Engineering* 5 (2017): 8192–8198, https://doi.org/10.1021/acssuschemeng.7b01839.

26. N. Wang, C. Ma, H. Yu, and X. Ji, "Thermodynamics of CO^2 Separation With the Superbase Derived Ionic Liquid – Organic Solvent Binary System," *Journal of Molecular Liquids* 331 (2021): 115760, https://doi.org/10.1016/j.molliq.2021.115760.

27. Y. Ansari, K. Ueno, and C. A. Angell, "Protic Ionic Liquids Can Be Both Free Proton Conductors and Benign Superacids," *The Journal of Physical Chemistry B* 125 (2021): 7855–7862, https://doi.org/10.1021/acs.jpcb.1c05299.

28. L. Wang, Y. Xu, Z. Li, Y. Wei, and J. Wei, "CO_2/CH_4 and H_2S/CO_2 Selectivity by Ionic Liquids in Natural Gas Sweetening," *Energy & Fuels* 32 (2018): 10–23, https://doi.org/10.1021/acs.energyfuels.7b02852.

29. H. Rodríguez and J. F. Brennecke, "Temperature and Composition Dependence of the Density and Viscosity of Binary Mixtures of Water + Ionic Liquid," *Journal of Chemical & Engineering Data* 51 (2006): 2145–2155, https://doi.org/10.1021/je0602824.

30. O. O. Okoturo and T. J. VanderNoot, "Temperature Dependence of Viscosity for Room Temperature Ionic Liquids," *Journal of Electroanalytical Chemistry* 568 (2004): 167–181, https://doi.org/10.1016/j.jelechem.2003.12.050.

31. D. Kaushik, P. Hitaishi, A. Kumar, D. Sen, S. M. Kamil, and S. K. Ghosh, "Temperature-Dependent Anomalous Viscosity of Aqueous Solutions of Imidazolium-Based Ionic Liquids," *Soft Matter* 19 (2023): 5674–5683, https://doi.org/10.1039/D3SM00333G.

32. E. Y. Tyunina, V. N. Afanasiev, and M. D. Chekunova, "Electroconductivity of Tetraethylammonium Tetrafluoroborate in Propylene Carbonate at Various Temperatures," *Journal of Chemical and Engineering Data* 56 (2011): 3222–3226.

33. M. Yoshizawa, W. Xu, and C. A. Angell, "Ionic Liquids by Proton Transfer: Vapor Pressure, Conductivity, and the Relevance of Δp Ka From Aqueous Solutions," *Journal of the American Chemical Society* 125 (2003): 15411–15419, https://doi.org/10.1021/ja035783d.

34. F. Gao, Z. Wang, P. Ji, and J. P. Cheng, "CO_2 Absorption by DBU-Based Protic Ionic Liquids: Basicity of Anion Dictates the Absorption Capacity

and Mechanism," *Frontiers in Chemistry* 6 (2019): 658, https://doi.org/10.3389/fchem.2018.00658.

35. D. Molino, G. Ferraro, S. Lettieri, et al., "Enhanced CO_2 Detection Using Potentiometric Sensors Based on PIM-1/DBU Imidazolate Membranes," *Advanced Sustainable Systems* 8 (2024): 2400415, https://doi.org/10.1002/adsu.202400415.

36. P. Rui, J. Xu, L. Zhao, et al., "Electrolyte Solutions: Measurement and Correlation of the Solubility of Et4NBF4 in Different Solvents at Temperatures From (263.15 to 323.15) K," *International Journal of Electrochemical Science* 15 (2020): 10221–10230, https://doi.org/10.20964/2020.10.26.

37. M. Oschatz, L. Borchardt, G. Hao, and S. Kaskel, *Nanocarbons for Advanced Energy Storage* (Wiley, 2015), 417–453, https://doi.org/10.1002/9783527680054.

38. F. Béguin, V. Presser, A. Balducci, and E. Frackowiak, "Carbons and Electrolytes for Advanced Supercapacitors," *Advanced Materials* 26 (2014): 2219–2251.

39. E. Y. Tyunina, M. D. Chekunova, and V. N. Afanasiev, "Electrochemical Characteristics of Propylene Carbonate Solutions of Tetraethylammonium Tetrafluoroborate," *Russian Journal of Electrochemistry* 49 (2013): 453–457.

40. H. V. T. Nguyen and K. K. Lee, "Tetraethylphosphonium Tetrafluoroborate Electrolyte for Paving the Way to Construct High-Power and High-Voltage Supercapacitors," *Journal of Energy Storage* 96 (2024): 112640, https://doi.org/10.1016/j.est.2024.112640.

Supporting Information

Additional supporting information can be found online in the Supporting Information section.

Supporting File: adsu70588-sup-0001-SuppMat.docx.